

# Drop-on-Demand Electrohydrodynamic Printing of Nematic Liquid Crystals

Waqas Kamal,<sup>\*</sup> Mengmeng Li, Thomas C. Sykes, Alfonso A. Castrejón-Pita,<sup>\*</sup> Steve J. Elston, and Stephen M. Morris<sup>\*</sup>

Electrohydrodynamic (EHD) printing of nematic liquid crystals (LCs) is demonstrated. Miniscule LC droplets, as small as 1 micron, are generated with the EHD printing system and deposited with high precision onto a glass substrate. Herein, we show how the voltage waveform and pulse frequency applied to the print nozzle influences the dynamics of the deposition process and the final landed footprint diameter of the printed spherical-cap-shaped LC droplets at the glass substrate. To complement results from high-speed shadowgraphy imaging, simulations are employed to model the jetting process and the formation of the Taylor cone. Using EHD printing, results for two different printing modes, cone jetting and microdripping, are shown. The benefits and drawbacks of each mode are highlighted, and the paper is concluded with the demonstration of a printed alphanumeric pattern that showcases the capability of EHD printing to deposit very small volumes of nematic LC in order to form well-defined spatial patterns.

## 1. Introduction

Due to their extraordinary electro-optic properties, liquid crystals (LCs) have been a topic of interest for both fundamental scientific research and technology development. In the latter case, this interest is most notably exemplified by the success of the flat panel LC display industry. Traditionally, research has focused on geometries and configurations where the LC is employed as a thin layer between a pair of glass substrates.<sup>[1–3]</sup> However, in recent years, there has been a growing interest in manufacturing LC droplet-like profiles for photonic technologies as they provide an interesting platform for generating new LC director profiles that can unlock novel optical and electro-optical


properties (e.g., microlens, optical vortex beam generation, and so on).<sup>[4–6]</sup> LC droplet-based technologies enable the LC director arrangement to be configured as a result of a combination of properties including the surface alignment conditions and importantly the droplet geometrical dimensions.<sup>[7–11]</sup>

To facilitate the degree of confinement (i.e., size of the LC droplet), modern microfluidic technologies have shown great potential in being able to produce a suspension of LC droplets, with droplet diameters ranging from 1 to 100  $\mu\text{m}$ , in the form of LC microspheres surrounded by an isotropic aqueous medium.<sup>[12–14]</sup> The potential of LC droplet-based systems has been demonstrated in diverse applications including chemical and biological sensors and optically driven LC rotators (optical

tweezers).<sup>[15–18]</sup> While being an effective means of generating uniform and regular-shaped droplets, these microfluidic approaches are typically limited in terms of fixing the droplets in position and creating well-organized periodic arrays of LC droplets.

In contrast, inkjet printing has emerged as a rapid prototyping tool for new LC photonics technologies due to its ability to precisely position picoliter volumes of functional fluids onto a variety of different substrates.<sup>[19–21]</sup> For instance, Alino et al. have demonstrated monodispersed LC droplets (diameters in the range of 35–136  $\mu\text{m}$ ) in aqueous solutions for chemical and biological sensing.<sup>[22]</sup> Separately, our group have explored the use of inkjet printing of nematic LCs to investigate the alignment of the director within sessile droplets<sup>[23]</sup> and further extended the technique to showcase the potential of printed LC droplets as thermally tunable microlenses.<sup>[24]</sup> Chiral nematic LCs have also been combined with printing techniques to form passive optical sensing devices. For example, Schenning et al. demonstrated a battery-free humidity and temperature sensors<sup>[25,26]</sup> as well as rewritable photonic coatings with the aid of inkjet printing of chiral nematic LC films.<sup>[27]</sup> Alternatively, Gardiner et al. reported the first printed LC lasers by inkjet printing dye-doped chiral nematic LC droplets onto a substrate that was pretreated with a wet polymer layer,<sup>[28]</sup> while Meng et al. demonstrated color changing films using inkjet printing technology and blue phase LCs.<sup>[29]</sup> Our group have also recently used inkjet printing to fabricate polymer-dispersed LC smart/privacy windows with embedded logos and images.<sup>[30,31]</sup> Very recently, Coppola et al. have

W. Kamal, M. Li, T. C. Sykes, A. A. Castrejón-Pita, S. J. Elston, S. M. Morris  
Department of Engineering Science  
University of Oxford  
Parks Road, Oxford OX1 3PJ, UK  
E-mail: waqas.kamal@eng.ox.ac.uk; alfonso.castrejonpita@eng.ox.ac.uk;  
stephen.morris@eng.ox.ac.uk

 The ORCID identification number(s) for the author(s) of this article can be found under <https://doi.org/10.1002/adem.202400245>.

© 2024 The Author(s). Advanced Engineering Materials published by Wiley-VCH GmbH. This is an open access article under the terms of the Creative Commons Attribution License, which permits use, distribution and reproduction in any medium, provided the original work is properly cited.

DOI: 10.1002/adem.202400245

reported the deposition of nematic LC droplets for microlens applications with sizes around 400  $\mu\text{m}$  using a pyro-electrohydrodynamic technique.<sup>[32]</sup>

A common feature in all of the aforementioned reports is that the in-flight LC droplet size was approximately equal to the size of the nozzle orifice from which the material was ejected, resulting in droplet footprint diameters on the substrate typically ranging from 30 to 400  $\mu\text{m}$ . In contrast to printing techniques where the material is pushed out of a nozzle (e.g., using a piezoelectric transducer), electrohydrodynamic (EHD) printing uses electric fields to extract liquid jets from a nozzle to deposit ultrasmall droplets onto a substrate, offering novel possibilities for fabricating micro/nanosized structures that overcomes the limits imposed by surface tension and viscosity when trying to deposit small droplets using inkjet printing.<sup>[33–36]</sup> Therefore, EHD printing presents the possibility of printing LC droplets with very small feature sizes that could lead to novel director profiles inside the LC droplets. In principle, this could be further exploited to manipulate certain LC ordering transitions for new LC droplet-based technologies. Moreover, EHD printing allows for high-resolution printing, i.e., a large number of droplets per square inch that extend well beyond what is accessible using traditional inkjet printing techniques.<sup>[37]</sup>

In the present work, we demonstrate the printing of LC droplets using an EHD printing technique and propose it as a potential method for manufacturing LC droplet-based devices that enable the generation of droplet sizes that are simply not possible with conventional inkjet and microfluidics-based droplet generation technologies. The key aims of this study are to demonstrate the Taylor cone formation of a nematic LC and show the effect of the characteristics of the voltage pulses on the single ejection of LC droplets to form patterns of sessile droplets in a drop-on-demand (DoD) fashion. Depending on the printing mode and voltage pulse characteristics, we demonstrate on-demand deposition of LC droplets with droplet diameters ranging from 1 to 30  $\mu\text{m}$ .

## 2. Experimental Section

### 2.1. The Electrohydrodynamic Printing System

The EHD printing system was developed in-house and is presented in Figure S1 and S2 in the Supporting Information. The nozzle consisted of prepulled borosilicate glass capillaries (sourced from World Precision Instruments) with outer diameters of either 1  $\mu\text{m}$  or 40  $\mu\text{m}$ . An electrical connection was made near the tapered end of the capillaries via copper foil tape that was carefully wrapped around the capillaries. A wire was subsequently attached to this copper “jacket” and the other end was connected to a shrouded banana plug, enabling an electrical signal to be delivered to the nozzle tip. A nematic LC was supplied to the glass capillary using PTFE tubing (PTFE microbore) connected to a syringe pump (PHD-70-3009) to deliver the fluid to the nozzle at the required flow rate.

A 61 mm  $\times$  61 mm silver sheet was used as the ground electrode that was firmly attached to a 3D printed 6 mm thick (same dimensions) poly(lactic acid) block, which served as an insulator. The whole assembly was then mounted on two

computer-controlled translation stages (MT1-Z8 Thorlabs), which were used to provide movement along the  $x$ - and  $y$ -axes over a range of 12 mm  $\times$  12 mm with  $\pm 1.5$   $\mu\text{m}$  accuracy. Each axis was controlled by a standalone motion controller (KDC101 Thorlabs), with the ability to output a signal describing each step. This output was used as an external input to trigger the printing process.

An arbitrary function generator (AFG 2021 Tektronix) was used to generate an input signal to the high-voltage amplifier (Trek 609 A) and an oscilloscope (TBS 1000 C Tektronix) was used to monitor the amplitude and frequency of the applied signal. The high-voltage amplifier, which could amplify the input signal by a factor of 1000 (resulting in output voltages in the range of 0–10 kV), was used to generate the large electric field amplitudes between the nozzle and the ground electrode needed for the development of the Taylor cone. Using this approach, it was possible to deposit droplets on-demand to form arbitrary spatial patterns and arrays.

A high-speed camera (Phantom v12.1 with a Navitar 12 $\times$  zoom lens) operating in a shadowgraphy configuration was used to monitor the space between the nozzle tip and the substrate. This enabled the printing process, including the Taylor cone formation, jet ejection, droplet formation, and deposition, to be monitored. Images were captured at 20–30 kfps with an image resolution of 512  $\times$  512 pixels.

### 2.2. The Liquid Crystal Ink

In this work, the nematic LC mixture BL006 (Merck) was chosen as the functional ink. This nematic LC was selected because it is liquid crystalline at room temperature and the nematic phase extends over a broad temperature range. This mixture has a positive dielectric anisotropy ( $\Delta\epsilon > 0$ ), which means for voltages greater than the Freedericksz threshold voltage ( $V_{th}$ ) the LC director (average molecular orientation) aligns in the direction of the applied electric field. When sandwiched as a thin layer between two electrodes, an electric field of 0.1–1  $\text{V}\mu\text{m}^{-1}$  is enough to completely reorient the LC director along the field direction. An EHD printing assembly typically delivers a large amplitude electric field of the order of 1  $\text{kV}\text{mm}^{-1}$ . Therefore, it can be assumed that during the EHD printing process, the LC director will align preferentially with the electric field direction and, as such, the component of the dielectric permittivity that is relevant in this case is  $\epsilon_{||}$ .

The material properties that are required to estimate the charge relaxation time, which is discussed in the following sections, are the relative dielectric permittivity ( $\epsilon_{||}$ ) and the electrical conductivity ( $\sigma$ ). For the nematic LC, BL006, the values of these properties at a temperature of 20  $^{\circ}\text{C}$  were found to be  $\epsilon_{||} = 22$  and  $\sigma = 10^{-10} \text{ Sm}^{-1}$ , respectively. The value of the dielectric permittivity was measured at a frequency of 1 kHz but does not vary significantly below this frequency. Table S1 in the Supporting Information provides the relevant material properties for BL006, obtained from the literature.

### 2.3. Characterization of EHD Printed Droplets

The printed LC droplets were characterized using a polarizing optical microscope (Olympus BX51). Microscopy was performed

in transmission whereby the illumination was provided by a halogen bulb. To perform polarized optical microscopy, two linear polarizers were placed such that their optical axes were orthogonal to each other, with images captured using a 14bit, 6.0 megapixel CCD camera (Retiga) mounted to the phototube of the microscope.

### 3. Results and Discussion

#### 3.1. Electrohydrodynamic Jetting of a Nematic Liquid Crystal

**Figure 1** presents a schematic of on-demand LC printing onto a lecithin-treated (homeotropic alignment layer) glass substrate. The diagram illustrates the generation of a pulsated cone jet to create a regular array of nematic LC droplets. To achieve single events of electrojetting (i.e., no satellite droplet formation or jet breakup), the square waveform shown in the figure was used, which consists of a pulsed voltage signal ( $V_p$ ) with a variable pulse width of time duration  $t_p$ . The pulse signal was superimposed on a DC bias voltage ( $V_b > 0$ ), thus resulting in a unipolar rectangular voltage signal being supplied to the nozzle tip. At the same time, the counter electrode was grounded ( $V_0 = 0$ ).

When a voltage pulse was applied, the meniscus of the LC transitioned into a cone-shaped structure pointing toward the surface before evolving into a jet of liquid that ejected from the apex of this cone. The jet then strikes the surface to form a printed sessile droplet. When the voltage pulse finishes, the jet disappears, and the cone retracts to the initial shape of a round meniscus at the orifice of the nozzle. The substrate is then translated to the next position where another droplet is to be

deposited. The Taylor cone formation process for a nematic LC is explained in more detail in Section 3.3. The dotted black box in the figure contains representative images of an LC droplet being EHD printed onto a homeotropic alignment glass substrate, and the schematic image illustrates the LC director configuration within a sessile LC droplet. The polarizing optical microscopy image reveals a dark center characterized by a Maltese cross pattern, indicating homeotropic alignment of the LC director throughout the printed droplet.<sup>[38]</sup> The four bright regions result from birefringence, which arises due to the slight tilt in the LC director induced by the curvature of the droplet.

#### 3.2. Simulations

Previous studies on the EHDs of weakly dielectric fluids have demonstrated that the process of surface deformation, involving the transition from a hemispherical meniscus to a cone shape, is initiated by minor surface perturbations. These perturbations, in turn, amplify the local electric field due to charge concentration, leading to an intensified electrostatic attraction. This cascading effect ultimately results in the formation of a cone, commonly referred to as the Taylor cone.<sup>[39]</sup>

**Figure 2a** presents a graphical illustration used as an example to illustrate the forces acting on the liquid cone when a fluid at the tip of a capillary is subjected to the applied electric field. For the purposes of simulations/modeling, we defined these forces using two separate physics modules in the COMSOL Multiphysics software and established a two-phase flow model with the level set method, using the governing equations detailed

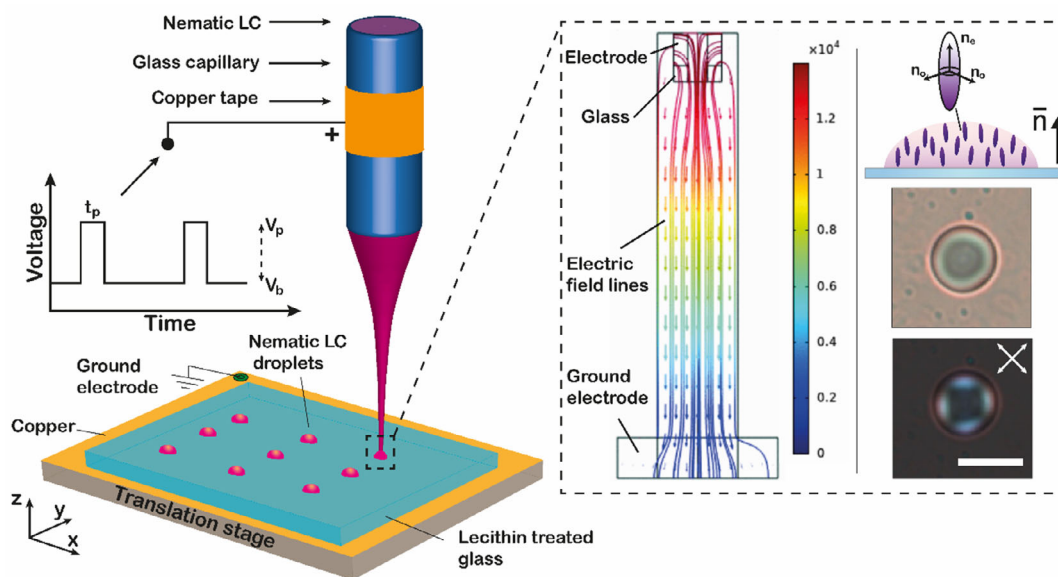


**Figure 1.** Schematic illustration of drop-on-demand EHD printing of nematic LCs. A pulsed DC voltage with regulated pulse width and repetition rate was applied between the nozzle and the substrate. Rectangular voltage pulses were superimposed on a bias voltage (DC offset). A schematic diagram of the applied waveform is shown, which consists of a bias voltage ( $V_b$ ), pulse voltage ( $V_p$ ), and pulse duration ( $t_p$ ). The inset image (within the dashed box) shows the simulated electric field lines when a voltage is applied between the nozzle and the ground electrode along with images on the right illustrating the director configuration in each droplet as well as polarizing optical microscope images of a single droplet (uncrossed polarizers—middle image; crossed polarizers—bottom image). The LC director is indicated by the unit vector  $\vec{n}$ , while  $n_o$  and  $n_e$  are, respectively, the ordinary and extraordinary refractive indices. The white double-headed arrows in the bottom right image in the dashed box indicate the orientations of the polarizers.

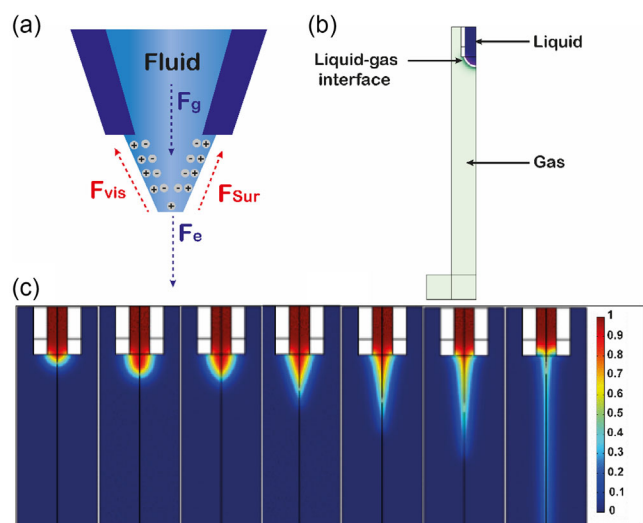


**Figure 2.** Simulations showing Taylor cone formation during the EHD deposition of a nematic LC. a) Diagram illustrating the forces that appear during the EHD Taylor cone formation process. Here, the electric forces ( $F_e$ ), due to the applied electric field, that develop at the LC jet are balanced by the surface tension ( $F_{sur}$ ), viscous force ( $F_{vis}$ ), and gravitational force ( $F_g$ ). b) Illustration showing the construction of the model employed to simulate nematic LC jet evolution using COMSOL. The model shows the liquid–gas interface used to track electrojetting. The liquid in this case is a nematic LC mixture (BL006) with dielectric permittivity parallel to LC director of  $\epsilon_{||} \approx 22$ . c) Simulated jet formation of a nematic LC at different time steps during the evolution from a meniscus through a Taylor cone to deposition onto the substrate. Here, a 40  $\mu\text{m}$  outer diameter nozzle placed at 1.1 mm height from the ground electrode and an applied voltage of 1.4 kV were used as the parameters in the simulation.

in ref. [37], alongside the material properties of the ink (see Table S1, Supporting Information) and air. We assumed incompressible and laminar fluid flows, and in order to reduce the computational complexity defined the nozzle geometry in a 2D-axisymmetric domain. The corresponding 2D model is shown in Figure 2b. The dark blue section represents the LC as an ink and the light green region represents the air, which is indicated as the gas phase, while the white section symbolizes the external wall of the glass nozzle. The nozzle's outer diameter was set as 40  $\mu\text{m}$  and the distance between the nozzle and the substrate was set as 1.1 mm under the application of an electric field of 1.4 kV.

Figure 2c presents a time series of images from simulations that shows the evolution of a liquid meniscus into a jet through the formation of a cone. This is a critical sequence in EHD printing under an applied electric field. Initially, the defined inlet velocity, which is imposed by the syringe pump in our experiment and set as a fixed velocity in our simulations, forces the liquid to exit the nozzle, culminating in the formation of a hemispherical meniscus at the apex of the nozzle due to a balance between the applied pressure and the liquid's surface tension. With the application of a voltage across the nozzle and the ground plane, the undisturbed meniscus experiences deformation under the influence of the electrostatic field. In turn, this applied electric field disrupts the surface tension balance, forcing

the meniscus to morph into a “Taylor cone,” which results from the equilibrium obtained between the competing electric and capillary forces.

### 3.3. Cone Jetting

Modeling the jetting process in COMSOL appears to show the formation of a Taylor cone. The next step was to demonstrate this process experimentally. In this case it was deemed essential to first understand the effect of the bias voltage on the formation and shape of the LC meniscus. For this, we performed a preliminary set of experiments to investigate the range of voltages at which the meniscus transitions into a state with increased fluid volume but without ejection of the droplets. This onset point is very important as it overcomes the effective surface tension of the hanging meniscus and helps to establish a smooth transition from the current state to the next.<sup>[40]</sup> For this purpose, a 40  $\mu\text{m}$  outer diameter glass nozzle was used, and the gap between the nozzle tip and substrate was set to 100  $\mu\text{m}$ . The LC was supplied to the tip of the nozzle using a syringe pump at a flow rate of 0.5  $\mu\text{L min}^{-1}$  while an electric field was applied between the nozzle and the ground electrode. It was observed that the LC drops started to eject in the form of large fluid filaments when the bias voltage was greater than 1 kV. Therefore, the DC bias voltage was thereafter kept in the range of 800–900 V.

Figure 3a illustrates the overall concept of single event electrojetting of a nematic LC where a meniscus, which is already subjected to the bias voltage, deforms into a cone directed toward the substrate surface when the pulse voltage is applied. This deformation is quickly followed by a jet of the liquid that is ejected from the apex of the cone. In the absence of a pulse voltage, the jet disappears and the cone returns to the shape of a meniscus. Experimentally, in order to generate a single LC droplet event, it was found that rectangular voltage pulses with 50 ms pulse duration at 1 s delay time in the range of 300–400 V had to be applied on top of the bias voltage. For a total voltage ranging from 1300 to 1400 V (bias voltage and the pulse voltage), the electrostatic force on the surface of the meniscus was sufficient to modify the meniscus into a conical shape, and subsequently to jet the LC from the apex of the cone. This process enabled the controlled extraction of a liquid jet to form a droplet.

Figure 3b presents a set of high-speed camera images of an LC jet formed at the capillary outlet. We estimated the apparent contact angle of the LC meniscus at the outlet of the capillary (nozzle) for both the field “off” and field “on” conditions using the shadowgraphy images presented in Figure 3b. In this case, the contact angle of the free meniscus (no electric field applied) and at jet formation (fifth shadowgraphy image) were found to be  $44^\circ \pm 2^\circ$  and  $66^\circ \pm 2^\circ$ , respectively. Note the similarity in the evolution of the jet with the results from simulations presented in Figure 2.

Our findings suggest that the mechanism responsible for the deposition of the LC in this case may not be the classical EHD atomization (EHDA) phenomenon. Materials with electrical conductivities in the range of  $10^{-3}$ – $10^{-6} \text{ Sm}^{-1}$  and a viscosity less than 150 mPa s have typically exhibited classical EHDA phenomenon,<sup>[41]</sup> as described by Melcher and Warren in 1971.<sup>[42]</sup> This phenomenon is attributed to the condition where the fluid

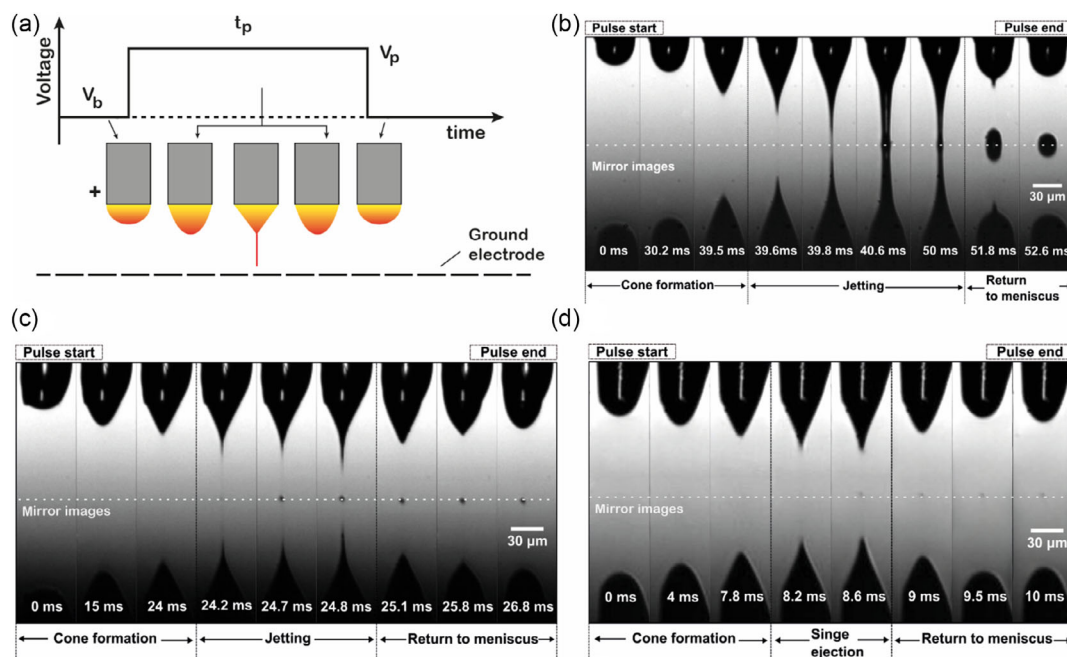


**Figure 3.** Effect of pulse width on fluid jet ejection from the Taylor cone. In this case EHD printing is onto lecithin-coated glass substrates resulting in a homeotropic alignment of the nematic LC. a) Schematic illustration of the offset that was added to the DC pulse that enabled Taylor cone formation and the fluid jet being stretched out to perform uniform-sized droplets. The offset is represented by a base voltage ( $V_b$ ) and the pulse amplitude is represented by  $V_p$ . High-speed shadowgraphy images of the jetting of the nematic LC BL006 captured using a high-speed camera (20 000 fps). The nozzle was a glass capillary with a 30  $\mu\text{m}$  internal diameter and 40  $\mu\text{m}$  outer diameter. The distance between the nozzle and the substrate was 100  $\mu\text{m}$ . The input waveform consisted of a  $V_b = 900$  V DC bias voltage, a pulse voltage of  $V_p = 300$  V, and a pulse frequency of  $f = 1$  Hz. The pulse duration in each case was: b) 50 ms, c) 25 ms, and d) 10 ms. The dotted white line is the reflection in each set of images. The printing was performed at a temperature of around 20  $^{\circ}\text{C}$ .

contains a sufficient number of charge carriers having a very short charge relaxation time ( $T_q$ ), typically in the range of  $10^{-7}$ – $10^{-5}$  s,<sup>[41]</sup> when compared with the fluid residence time, which is commonly referred to as the hydrodynamic relaxation time ( $T_h$ ), at the nozzle orifice. In contrast, nematic LCs, such as BL006, typically have very low electrical conductivity ( $10^{-10}$   $\text{Sm}^{-1}$ , see Table S1, Supporting Information) that would correlate with a charge relaxation time ( $T_h$ ) of 1.94 s which is clearly very long and hence does not appear to be consistent with the time-scales required for classical EHDA phenomenon. Deposition of low conductivity fluids have been demonstrated previously. For example, a study by Jayasinghe et al. conducted on silicon oil, which had a very low conductivity of  $10^{-12}$   $\text{Sm}^{-1}$  and viscosity in the range of  $10^2$ – $10^4$  mPa s, observed that micron-sized threads did detach from an elongated Taylor cone.<sup>[43,44]</sup>

### 3.4. Effect of Frequency

In the next section, we will consider the timescale over which a nematic LC cone can dispense a jet by applying a series of pulses with a defined pulse duration time and delay. The pulse duration and the delay between two consecutive pulses are critical parameters that significantly influence the DoD EHD printing process. Figure 3b–d presents images captured by the high-speed camera at the three different pulse duration times of 50, 25, and 10 ms, where the nozzle was subjected to a 300 V pulse voltage and a 900 V DC bias voltage. In this case, the pulse frequency was

set to 1 Hz. For a pulse duration time of 50 ms, large thick fluid ligaments were observed (Figure 3b). The thickness of the jet (40 ms frame, Figure 3b) was found to be of the order of 10  $\mu\text{m}$ . However, when the pulse duration was reduced to either 25 ms or 10 ms, we observed thinner fluid jets with a jet thickness in the submicron range, as depicted in Figure 3c,d, respectively. In addition, it was possible to perform jetting at 5 ms pulse duration, although below 5 ms there was no discernible movement of the meniscus, and no jet was observed. (The effect of pulse duration time on the size of the droplet is discussed in the next section.) We observed that LC jets were highly reproducible at a pulse frequency of 1 Hz. However, at frequencies between 2 and 4 Hz, LC jetting became sporadic, and above 4 Hz, no jetting was observed. This observation suggests that at lower pulse frequencies, i.e., less than 2 Hz, the electric field stresses are highly reproducible in jet formation. The primary cause for the frequency-dependent LC jetting is believed to be due to the charge relaxation time, which for the LC ink is of the order of seconds (as discussed in the previous paragraph). Consequently, when the pulse frequencies exceeded 2 Hz, the free charges at the LC tip do not build up sufficiently leading to intermittent jetting. Likewise, at even higher pulse frequencies, greater than 4 Hz, the time it takes for the charges to relax is much shorter, of the order of milliseconds, while the reaction time of the LC remains of the order of seconds. Therefore, it is believed that this mismatch in timescales is responsible for no jetting being observed.

### 3.5. Effect of Pulse Duration

In order to further investigate the effect of pulse duration time on droplet sizes, the jetting process (seen in Figure 3 using 40  $\mu\text{m}$  outer diameter) was carried out onto a lecithin-coated glass substrate to facilitate the formation of sessile LC droplets. The substrate preparation process has already been described in the Experimental Section. **Figure 4a** shows optical microscope images of different sized droplets printed at 5, 10, 15, 25, and 50 ms pulse duration times and with a 40  $\mu\text{m}$  outer diameter glass capillary. Printing was performed at 1 Hz pulse frequency and it was observed that the drop generation rate was similar to the input pulse frequency. The plot in **Figure 4b** shows the corresponding landed droplet footprint diameters as a function of the width of the voltage pulse (in milliseconds). It is evident that the pulse duration time greatly influenced the droplet size. Here, for a 5 ms pulse duration, the minimum droplet footprint diameter was found to be  $8 \pm 1 \mu\text{m}$  whereas the maximum landed footprint diameter was recorded for a 50 ms pulse duration and was found to be  $30 \pm 2 \mu\text{m}$ . The effect of pulse duration on droplet diameter is in accordance with the behavior reported previously for both conductive and nonconductive inks.<sup>[45–47]</sup> As the entire EHD printing process was conducted at room temperature and standard atmospheric pressure, we do not anticipate any potential instability caused by such external factors on the droplet profiles after the printing process has been completed.<sup>[48,49]</sup> This is because the shape of the droplets is determined by the interplay between the interfacial tension, gravitational force, and droplet size. The droplet sizes presented in this work are consistently less than 1 mm, where surface tension forces dominate compared to other external factors such as atmospheric pressure and the gravitational force. On the other hand, the minimum EHD printed droplet diameter reported here is around 1  $\mu\text{m}$ , which is 10 times greater than the size of the droplets (100 nm) where intermolecular forces come into effect, dominating over any interfacial forces, and potentially leading to droplet instabilities.<sup>[50–52]</sup>

For EHD printing with conductive materials, droplets deposited on the substrate can accumulate charges, altering the substrate's electrical properties. This phenomenon may affect droplet spreading, adhesion, and ultimately, the morphology and deposition pattern. To mitigate this issue, it is crucial to ground the substrate, providing a pathway for excess charges to dissipate, minimizing their influence on the printed materials. Moreover, when using dielectric materials such as LCs in EHD printing, the likelihood of significant charge accumulation is reduced. Dielectric materials exhibit poor electrical conductivity, resulting in minimal charge storage and redistribution rather than buildup. Consequently, the impact of electric fields on micro–nanopatterning is expected to be less significant with dielectric materials. Furthermore, the LC droplets can still provide dielectric coupling and function effectively within devices when driven by externally applied electric potentials.

### 3.6. On-Demand Deposition

To investigate on-demand droplet deposition, in the cone-jet mode, we employed the 40  $\mu\text{m}$  outer diameter nozzle and also a 1  $\mu\text{m}$  inner diameter glass capillary, which were both used to print nematic LC droplets in the form of arrays. **Figure 5a** shows an optical microscope image of an array of LC droplets that were printed with the 40  $\mu\text{m}$  outer diameter glass nozzle on a lecithin-treated glass substrate. In this droplet patterning, we utilized the output signal from the controller of the motorized stages as an external input to trigger the high-voltage amplifier that, in turn, powered the printing nozzle. This method refers to the case of moving-a-step and print, which provides an efficient way to create a uniform coverage of droplets over the substrate. The microscopy image shows that the droplets are uniform in shape and have a footprint diameter of 8  $\mu\text{m}$  with  $\pm 1 \mu\text{m}$  variation. **Figure 5b** shows results for the case when printing on-demand deposition was performed with the 1  $\mu\text{m}$  inner diameter glass capillary. It can be seen that the jet was ejected at each input pulse on the substrate forming a  $4 \times 6$  array of droplets. The

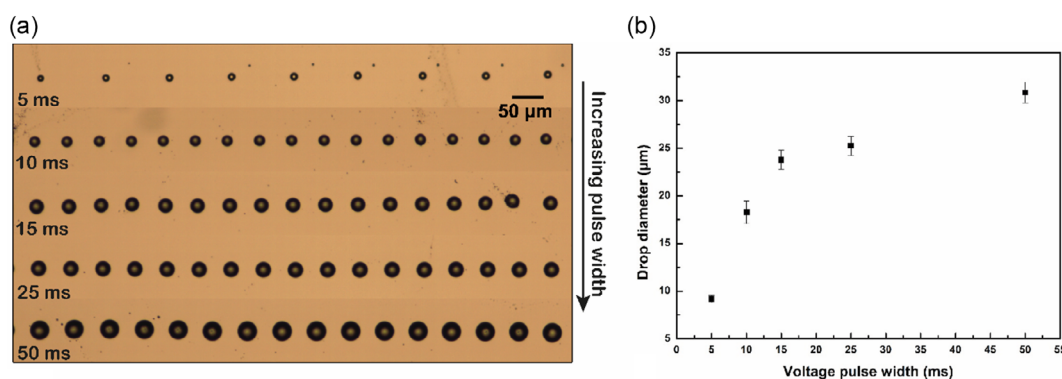


**Figure 4.** Controlling the size of an EHD printed nematic LC droplet. Printing was performed with a 40  $\mu\text{m}$  outer diameter nozzle. a) The effect of increasing the pulse width of the voltage waveform on the resulting droplet footprint diameter. Optical microscope image of nematic LC (BL006) droplets deposited using EHD printing onto a glass substrate with a homeotropic alignment layer. The distance between the nozzle and substrate was 100  $\mu\text{m}$ , and the substrate was translated at very low speeds (less than  $1 \text{ mm s}^{-1}$ ) during the printing process to form rows of droplets. Note that the substrate speed was not constant for all rows of droplets. b) The effect of the pulse duration on the resulting nematic LC droplet footprint diameter. The input print conditions were a DC bias voltage of  $V_b = 900 \text{ V}$ , a pulse voltage of  $V_p = 300 \text{ V}$ , a pulse frequency of  $f = 1 \text{ Hz}$ , and a flow rate of  $0.5 \mu\text{L min}^{-1}$ .

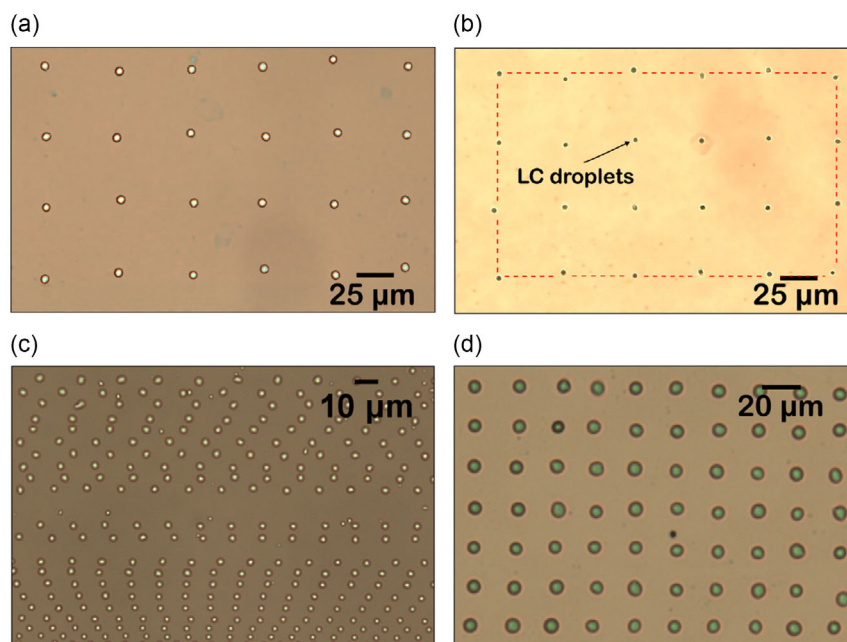


**Figure 5.** Cone-jet mode EHD printing. Optical microscope images of printed square arrays of nematic LC droplets when printing was performed in the cone-jet mode as schematically illustrated and experimentally shown in Figure 3. The nozzle sizes used were a) 40  $\mu\text{m}$  and b–d) 1  $\mu\text{m}$ . In (a) and (b), the EHD jet was triggered by the leading edge of the output signal from the motion controller and this mode of printing is termed “on-demand” EHD printing. For (c) and (d), the jet was triggered internally at a frequency of 4 Hz and the translation stages were moved at speeds less than 1  $\text{mm s}^{-1}$ . The operating conditions for (a) were a DC bias voltage of  $V_b = 900$  V, a pulse voltage of  $V_p = 300$  V, a pulse frequency of  $f = 1$  Hz, a pulse width of 5 ms, and a flow rate of  $0.5 \mu\text{L min}^{-1}$ . The operating conditions for (b–d) were  $V_b = 1000$  V,  $V_p = 400$  V, and the nematic LC volume flow rate was set to  $0.1 \mu\text{L min}^{-1}$ . The pulse durations were a) 5 ms and b) 2 ms, while in (c) and (d) they were 1–10 and 3 ms, respectively. The distance between the nozzle and glass substrate was 100  $\mu\text{m}$ .

footprint size of each droplet was found to be around 1–2  $\mu\text{m}$  in diameter. The red dotted lines superimposed over the image are used to highlight the positional deviation of the printed droplets, which was around  $\pm 1.5 \mu\text{m}$  and is in accordance with the positional accuracy of the translation stages.

We performed a set of printing trials to identify the conditions required to dispense the LC jet to form the droplets. When the LC reached the tip, the syringe pump was adjusted to run at the desired ink flow rates. Prior to the printing process, the nozzle and syringe pump assembly were left for a period of time to dissipate any residual back pressure that might have been produced due to an expansion of the PTFE tube. As the 1  $\mu\text{m}$  inner diameter capillaries were dominated by capillary forces, a lower DC bias voltage did not result in jetting. Instead, a DC bias voltage in the range of 950–1000 V and a pulse voltage in the range 300–400 V were required. The volume flow rate of the syringe pump was fixed at  $0.1 \mu\text{L min}^{-1}$ .

Figure 5c shows an optical micrograph of the printed droplets when the nematic LC was printed when the pulse time duration was varied between 1 and 10 ms at a fixed pulse frequency of 4 Hz. Here, the motion stages were translated at arbitrary speeds but always less than  $1 \text{ mm s}^{-1}$ . In the image, the bottom rows of droplets correspond to the case when the pulse duration time is in the range of 1–5 ms while the upper rows correspond to pulse durations of the order of 5–10 ms. The footprint size of the printed droplets was found to be in the range of 1–3  $\mu\text{m}$ .

These results indicate that nematic LC jets exhibit high reproducibility when utilizing a 1  $\mu\text{m}$  inner diameter glass capillary, even at pulse frequencies of up to 4 Hz, which was not the case when printing was carried out with a 40  $\mu\text{m}$  outer diameter glass capillary.

To achieve a regular array of droplets in a drop-on-demand fashion, the nozzle was operated at a pulse frequency of 4 Hz with a 3 ms pulse duration, and the translation stage was translated at around  $800 \mu\text{m s}^{-1}$ . Figure 5d demonstrates a more uniform array of LC droplets, with droplet footprint diameters of  $\approx 3 \mu\text{m}$ . Additionally, an attempt was made to explore drop-on-demand EHD printing at a 10 Hz pulse frequency. However, at this frequency, intermittent jetting was observed, resulting in the deposition of droplets with irregular shapes and sizes (see Figure S3 in the Supporting Information). Consequently, these findings suggest that with a 1  $\mu\text{m}$  inner diameter glass capillary, drop-on-demand printing can be conducted with EHD printing in the cone-jet mode with pulse frequencies ranging from 1 to 4 Hz and pulse durations spanning from 1 to 3 ms using the current EHD printing assembly.

### 3.7. Microdripping Mode

Even though it has been demonstrated that a nematic LC can undergo EHD jetting to produce micron-sized droplets, the cone-jet mode only appeared to function for a limited range of

input pulse frequencies. For example, in our printing trials with a 40  $\mu\text{m}$  outer diameter glass nozzle, stable cone jetting was only observed when the input pulse frequencies were less than 2 Hz. This limitation is not ideal for the printing of large arrays or periodic structures as it will lead to very long fabrication times. Another EHD printing mode, known as the microdripping mode, offers higher throughput and controlled micron-sized droplet formation that generally appears at the onset of the cone-jet mode, i.e., at comparatively low electric potential and low volume flow rate. This printing mode, as illustrated in **Figure 6**, has been reported to lead to a high throughput and controlled micron-sized droplet deposition for a range of liquids, especially for dielectrics/poorly conductive inks that are often unable to undergo Taylor cone jetting.<sup>[45,50]</sup>

In order to create large number of droplets with greater uniformity, EHD printing was therefore performed in the microdripping mode using the same experimental configuration as for the cone-jetting mode. The 40  $\mu\text{m}$  outer diameter glass capillary was preferred in this case because it was possible to image the printing dynamics at the tip of the nozzle. For the microdripping mode printing, the operating parameters optimized for the 40  $\mu\text{m}$  outer diameter (for the cone-jet mode) nozzle were used as an initial basis for the experiments. The reduction in electric field strength was found to be the key factor in performing microdrip EHD printing. Therefore, to reduce the electric field strength, the distance between the nozzle and the substrate was increased (from 100  $\mu\text{m}$ ) by moving the printhead along the z-direction (upward).

**Figure 7** shows an example image of LC microdripping from a 40  $\mu\text{m}$  outer diameter glass capillary with a nozzle height of 300  $\mu\text{m}$ . To perform microdripping, small adjustments were made to the DC bias voltage and pulse voltage amplitudes. Specifically, the bias voltage,  $V_b$ , was reduced to 800 V whereas the pulse voltage,  $V_p$ , was increased to 600 V. Additionally, the pulse width was set to 5 ms and the volume flow rate used was 1  $\mu\text{L min}^{-1}$ . As can be seen in the fourth frame (3.5 ms) of **Figure 7**, the resulting forces elongate the apex of the cone to create a liquid filament, which then undergoes necking and detaches a micron-sized droplet. The remaining filament returns to the main meniscus (sixth frame, 4.3 ms). Due to the constant volume flow rate, the height of the meniscus remains unchanged, as can be seen in the first and last frames of **Figure 7**. For pulse widths >10 ms it was observed that large fluid filaments were formed, which resulted in the formation

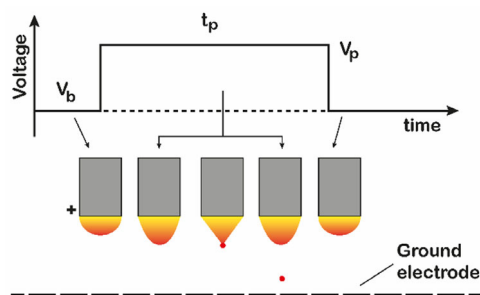


**Figure 6.** Microdripping mode. Illustration of the microdripping EHD printing mode of a nematic LC.

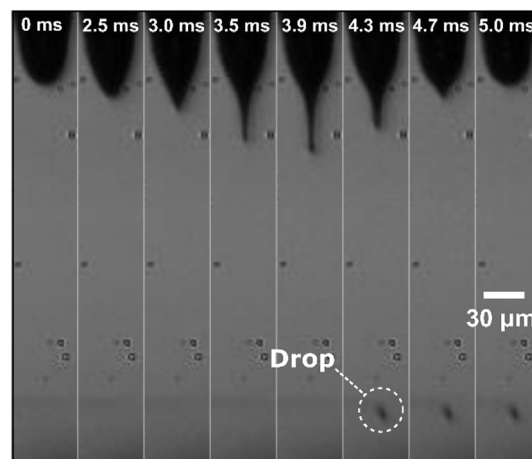


**Figure 7.** EHD printing of nematic LC in the microdripping mode. High-speed shadowgraphy images showing EHD printing of a nematic LC (BL006) in the microdripping mode. The height between the nozzle and substrate was 300  $\mu\text{m}$ . The nozzle size was 40  $\mu\text{m}$  outer diameter and the input waveform consisted of a  $V_b = 800$  V,  $V_p = 600$  V, and pulse duration of 5 ms. The volume flow rate was set to 1  $\mu\text{L min}^{-1}$  and the printing was performed at a temperature of 20  $^{\circ}\text{C}$ .

of large globules and irregular-shaped droplet artifacts on the substrate.

Using the operating conditions mentioned above, nematic LC droplets formed by the microdripping mode were deposited as an array covering a size of 600  $\times$  600  $\mu\text{m}^2$  (see **Figure 8a**). The droplets were printed at 10 Hz pulse frequency on a lecithin-treated glass substrate. The enlarged image in **Figure 8b** shows that the drops are consistent in terms of landed droplet shape with very little variation in the quality of the droplet boundary and diameter. **Figure 8c** shows the resulting histogram of droplet diameters for 600 printed droplets. The average droplet diameter was found to be 8.5  $\mu\text{m}$  (mean) with a standard deviation of 0.43  $\mu\text{m}$ , assuming a normal distribution. These drops are 14 times smaller than those fabricated using inkjet printing, which provides a remarkable opportunity to fabricate printed LC devices with droplet sizes less than 10 microns.<sup>[21,24]</sup>

### 3.8. EHD Printed Liquid Crystal Patterns

The EHD printing system can be used to assemble droplets to form various images/logos/patterns by instructing the translation stages to move in any direction using a script that can generate arrays and circles, as well as print alphanumeric characters. To demonstrate this capability, we performed on-demand droplet deposition to form alphanumeric characters “SMP” and a rectangular array of droplets (see **Figure S4** in the Supporting Information). In addition, an example image of the far-field diffraction pattern of an EHD-printed 2D droplet array designed to act as a diffractive optic element is presented in **Figure S5** in the Supporting Information.

**Figure 9a** presents an optical microscope image of the letters that were printed using the 40  $\mu\text{m}$  outer diameter nozzle in the microdripping mode. It can be seen in **Figure 9a** that the droplets are homogenous with an average footprint diameter of 8  $\mu\text{m}$  and a distance between the droplets of 50  $\mu\text{m}$ . Additionally, **Figure 9b**

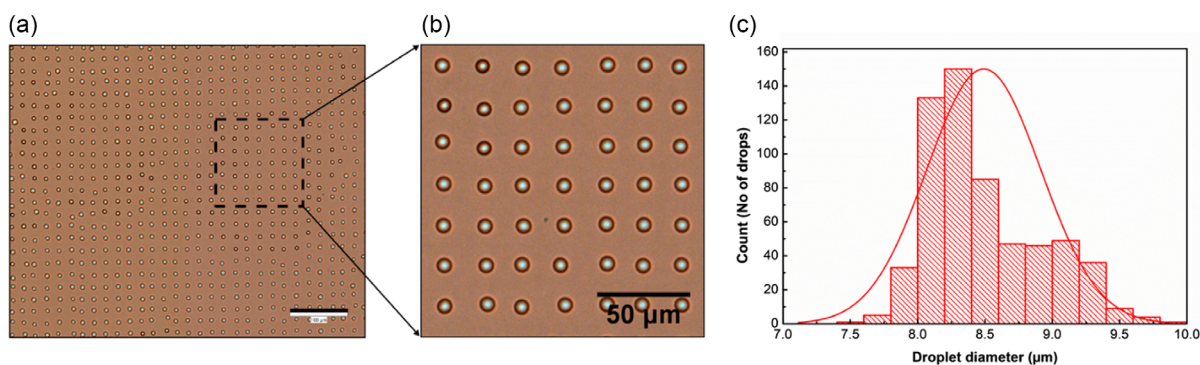


**Figure 8.** EHD printing in the microdripping mode. a) Optical microscopy image showing a 2D array of EHD printed nematic (BL006) LC droplets printed onto a lecithin-coated glass substrate. EHD printing was conducted in the microdripping mode with a 40 μm outer diameter glass nozzle. b) Enlarged region of the array in (a). c) Histogram plot showing the variation in the landed droplet footprint diameter of 600 EHD printed droplets. The red curve is a normal distribution fit to the experimental data.

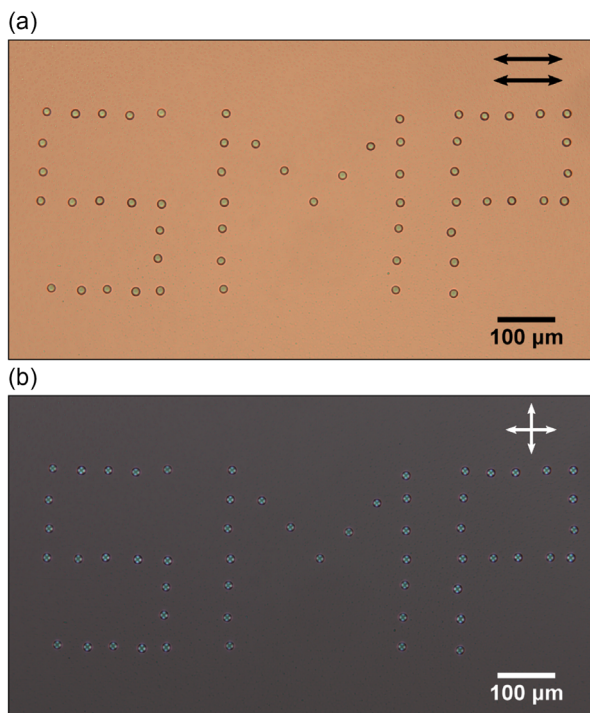


**Figure 9.** EHD printing of patterns using the microdripping mode. Polarizing optical microscope images of an EHD-printed alphanumeric logo using a nematic LC. a) Image taken with parallel polarizers (the orientations of the polarizers are denoted by the double-headed black arrows) and b) image taken with crossed polarizers (the orientations are denoted by the white double-headed arrows). The nematic LC was EHD printed with a 40 μm outer diameter glass capillary onto a lecithin-coated glass substrate. The distance between the nozzle and substrate and the syringe pump volume flow rate were set to 100 μm and 1 μL min<sup>-1</sup>, respectively. The input waveform consisted of  $V_b = 800$  V,  $V_p = 600$  V, and pulse duration of 5 ms. The printing was performed at a temperature of 20 °C.

shows a polarizing optical microscope image with crossed polarizers. Every droplet shows the four bright quadrants as shown previously in Figure 1, which indicates a near-homeotropic alignment of the LC director field inside the spherical cap droplets.

## 4. Conclusions

In conclusion, we have demonstrated the EHD printing of a nematic LC, which enables diminutive droplets to be generated and deposited onto glass substrates with potential applications in photonics and other technologies. Shadowgraphy imaging indicates the formation of a Taylor cone that leads to the ejection of a jet of LC and the subsequent placement of a spherical cap droplet onto a glass substrate coated with a homeotropic alignment layer. By studying the effects of pulse duration time and pulse repetition rates, we have identified two distinct printing modes, referred to as cone jetting and microdripping, providing different routes for printing droplets on-demand.

By conducting printing in the cone-jet mode with 40 and 1 μm outer diameter nozzles, we have successfully printed arrays of droplets with footprint diameters ranging from 1 to 30 μm. For each nozzle, it was found that the size of the droplets was directly related to the pulse duration time and frequency. Using shorter pulse duration times (between 1 and 5 ms) and lower pulse frequencies (less than 4 Hz), we observed increased control over droplet size and quality. However, while stable and reproducible LC jets are achievable when printing in the cone-jet mode, it may not be suitable for large-scale droplet arrays.

In contrast, the microdripping mode exhibited greater control in terms of increasing printing speed. Using a 40 μm outer diameter nozzle, we have successfully printed droplets with a footprint diameter of 8.5 μm, 4 or 5 times smaller than the nozzle diameter, at a pulse frequency of 10 Hz. These results indicate the potential applicability of EHD printing in the deposition of very small volumes of liquid crystalline materials to form arrays and patterns to realize new optic and photonics components and technologies. The approach also enables the study of the LC director profile in very confined geometries. Other areas for further study include assessing the focusing characteristics of these EHD-printed micro/nanolenses as well as the printing of LC materials mixed with polymers to form large-area arrays that could then be manipulated by an applied electric field to act as micro/nanolight shutters.

## Supporting Information

Supporting Information is available from the Wiley Online Library or from the author.

## Acknowledgements

W.K. acknowledges the financial support provided by Punjab Educational Endowment Fund (PEEF), Pakistan. A.A.C.–P. was supported by the Royal Society through a University Research Fellowship (URF\R\180016) and the John Fell Fund, Oxford University Press, via the Pump-Priming grants (0005176) and (0005519). C.H acknowledges financial support from St John's College (Oxford) for a Junior Research Fellowship.

## Conflict of Interest

The authors declare no conflict of interest.

## Data Availability Statement

The data that support the findings of this study are available from the corresponding author upon reasonable request.

## Keywords

electrohydrodynamic printing, microdripping, nematic liquid crystals, optical devices, Taylor cone jetting

Received: January 30, 2024

Revised: April 9, 2024

Published online: May 25, 2024

- [1] G. H. Heilmeyer, L. A. Zanoni, L. A. Barton, *Proc. IEEE* **1968**, 56, 1162.
- [2] S. M. Kelly, M. O'Neill, *Handbook of Advanced Electronic and Photonic Materials and Devices*, Vol. 7, [https://www.google.com/search?sca\\_esv=9eeb101476a64b32&sca\\_upv=1&rlz=1C1GCEU\\_eniN1078IN1078&q=Amsterdam&si=ACC90nyZndfSpHALIN52qAqIQZE2s8nxEbc9OSW3bjf5\\_eZmaoei\\_cuHAxMYiGt6nk2fguopwCS\\_7hRfwrjxGpAvopEcGDAxCD\\_RVgbu6ONDDWrc7qsF52rFZjTBA2RBFdu1MfhWSSsOgtiDcxPxl9zM7BpL5TSkdWODLGNjOfjX7lLs4GRtCN72wLsW3LuF\\_ZMr60&sa=X&ved=2ahUKEwj\\_k\\_ez68l-GAxVLRVYBHZQEucQmxMoAXoECfkQAw](https://www.google.com/search?sca_esv=9eeb101476a64b32&sca_upv=1&rlz=1C1GCEU_eniN1078IN1078&q=Amsterdam&si=ACC90nyZndfSpHALIN52qAqIQZE2s8nxEbc9OSW3bjf5_eZmaoei_cuHAxMYiGt6nk2fguopwCS_7hRfwrjxGpAvopEcGDAxCD_RVgbu6ONDDWrc7qsF52rFZjTBA2RBFdu1MfhWSSsOgtiDcxPxl9zM7BpL5TSkdWODLGNjOfjX7lLs4GRtCN72wLsW3LuF_ZMr60&sa=X&ved=2ahUKEwj_k_ez68l-GAxVLRVYBHZQEucQmxMoAXoECfkQAw) Elsevier, Amsterdam **2001**, pp. 1–66.
- [3] H. Chen, J. He, S.-T. Wu, *IEEE J. Sel. Top. Quantum Electron.* **2017**, 23, 1.
- [4] G. Posnjak, *Topological Formations in Chiral Nematic Droplets*, Springer International Publishing, Cham **2018**, pp. 29–39.
- [5] Y. Li, J. Jun-Yan Suen, E. Prince, E. M. Larin, A. Klinkova, H. Thérien-Aubin, S. Zhu, B. Yang, A. S. Helmy, O. D. Lavrentovich, E. Kumacheva, *Nat. Commun.* **2016**, 7, 12520.
- [6] K. Peddireddy, S. Čopar, K. V. Le, I. Mušević, C. Bahr, V. S. R. Jampani, *Proc. Natl. Acad. Sci.* **2021**, 118, e2011174118.
- [7] D. A. Paterson, P. Bao, R. H. Abou-Saleh, S. A. Peyman, J. C. Jones, J. A. T. Sandoe, S. D. Evans, H. F. Gleeson, R. J. Bushby, *Langmuir* **2020**, 36, 6436.
- [8] D. S. Miller, N. L. Abbott, *Soft Matter* **2013**, 9, 374.
- [9] V. Tomar, S. I. Hernández, N. L. Abbott, J. P. Hernández-Ortiz, J. J. de Pablo, *Soft Matter* **2012**, 8, 8679.
- [10] O. D. Lavrentovich, *Liq. Cryst.* **1998**, 24, 117.
- [11] M. Urbanski, C. G. Reyes, J. Noh, A. Sharma, Y. Geng, V. Subba Rao Jampani, J. P. F. Lagerwall, *J. Phys.: Condens. Matter* **2017**, 29, 133003.
- [12] J.-W. Kim, S. H. Han, Y. H. Choi, W. M. Hamonangan, Y. Oh, S.-H. Kim, *Lab Chip* **2022**, 22, 2259.
- [13] Z. Nie, M. Seo, S. Xu, P. C. Lewis, M. Mok, E. Kumacheva, G. M. Whitesides, P. Garstecki, H. A. Stone, *Microfluid. Nanofluidics* **2008**, 5, 585.
- [14] T. Moragues, D. Argüjo, T. Beneyton, C. Modavi, K. Simutis, A. R. Abate, J.-C. Baret, A. J. Demello, D. Densmore, A. D. Griffiths, *Nat. Rev. Methods Prim.* **2023**, 3, 32.
- [15] P. Bao, D. A. Paterson, P. L. Harrison, K. Miller, S. Peyman, J. C. Jones, J. Sandoe, S. D. Evans, R. J. Bushby, H. F. Gleeson, *Lab Chip* **2019**, 19, 1082.
- [16] K. Saito, Y. Kimura, *Sci. Rep.* **2022**, 12, 16623.
- [17] T. A. Wood, H. F. Gleeson, M. R. Dickinson, A. J. Wright, *Appl. Phys. Lett.* **2004**, 84, 4292.
- [18] S. Juodkazis, M. Shikata, T. Takahashi, S. Matsuo, H. Misawa, *Jpn. J. Appl. Phys.* **1999**, 38, L518.
- [19] W. Kamal, A. C. J. Orr, T. C. Sykes, A. A. Castrejón-Pita, S. J. Elston, S. M. Morris, *Mater. Today Adv.* **2023**, 19, 100416.
- [20] T. R. Cull, M. J. Goulding, M. Bradley, *Adv. Mater.* **2007**, 19, 2355.
- [21] W. Kamal, J. Lin, S. J. Elston, T. Ali, A. A. Castrejón-Pita, S. M. Morris, *Adv. Mater. Interfaces* **2020**, 7, 2000578.
- [22] V. J. Aliño, K. X. Tay, S. A. Khan, K.-L. Yang, *Langmuir* **2012**, 28, 14540.
- [23] E. Parry, D.-J. Kim, A. A. Castrejón-Pita, S. J. Elston, S. M. Morris, *Opt. Mater.* **2018**, 80, 71.
- [24] E. Parry, S. Bolis, S. J. Elston, A. A. Castrejón-Pita, S. M. Morris, *Adv. Eng. Mater.* **2018**, 20, 1700774.
- [25] J. E. Stumpel, C. Wouters, N. Herzer, J. Ziegler, D. J. Broer, C. W. M. Bastiaansen, A. P. H. J. Schenning, *Adv. Opt. Mater.* **2014**, 2, 459.
- [26] W. Zhang, A. A. F. Froyen, A. P. H. J. Schenning, G. Zhou, M. G. Debije, L. T. De Haan, *Adv. Photonics Res.* **2021**, 2, 2100016.
- [27] M. Moirangthem, A. F. Scheers, A. P. H. J. Schenning, *Chem. Commun.* **2018**, 54, 4425.
- [28] D. J. Gardiner, W.-K. Hsiao, S. M. Morris, P. J. W. Hands, T. D. Wilkinson, I. M. Hutchings, H. J. Coles, *Soft Matter* **2012**, 8, 9977.
- [29] F. Meng, C. Zheng, W. Yang, B. Guan, J. Wang, T. Ikeda, L. Jiang, *Adv. Funct. Mater.* **2022**, 32, 2110985.
- [30] W. Kamal, M. Li, J.-D. Lin, E. Parry, Y. Jin, S. J. Elston, A. A. Castrejón-Pita, S. M. Morris, *Adv. Opt. Mater.* **2021**, 10, 2101748.
- [31] M. Li, W. Kamal, A. C. J. Orr, A. A. Castrejón-Pita, S. J. Elston, S. M. Morris, *Macromol. Chem. Phys.* **2022**, 223, 2200154.
- [32] S. Coppola, V. Vespini, J. Behal, V. Bianco, L. Miccio, L. De Sio, P. Ferraro, *ACS Appl. Mater. Interfaces* **2024**, 16, 19453.
- [33] W. Kamal, K. Rahman, S. Ahmad, M. Shakeel, T. Ali, *Flex. Print. Electron.* **2022**, 7, 045008.
- [34] Y. Han, J. Dong, *J. Micro Nano-Manuf.* **2018**, 6, 040802.
- [35] B. Zhang, J. He, X. Li, F. Xu, D. Li, *Nanoscale* **2016**, 8, 15376.
- [36] J.-U. Park, M. Hardy, S. J. Kang, K. Barton, K. Adair, D. Mukhopadhyay, C. Y. Lee, M. S. Strano, A. G. Alleyne, J. G. Georgiadis, P. M. Ferreira, J. A. Rogers, *Nat. Mater.* **2007**, 6, 782.
- [37] H. Wang, Y. Zhang, Y. Liu, Z. Chen, Y. Li, X. Li, X. Xu, *Nanoscale Adv.* **2023**, 5, 1183.
- [38] J. Yoshioka, K. Fukao, *Phys. Rev. E* **2019**, 99, 022702.
- [39] N. Mkhize, H. Bhaskaran, *Small Sci.* **2022**, 2, 2100073.
- [40] K.-S. Kwon, D.-Y. Lee, *J. Micromech. Microeng.* **2013**, 23, 65018.
- [41] A. Lee, H. Jin, H.-W. Dang, K.-H. Choi, K. H. Ahn, *Langmuir* **2013**, 29, 13630.
- [42] A. M. Gañán-Calvo, *J. Fluid Mech.* **1997**, 335, 165.
- [43] H. B. Zhang, M. J. Edirisinghe, S. N. Jayasinghe, *J. Fluid Mech.* **2006**, 558, 103.
- [44] S. N. Jayasinghe, M. J. Edirisinghe, *J. Aerosol Sci.* **2004**, 35, 233.

- [45] M. W. Lee, D. K. Kang, N. Y. Kim, H. Y. Kim, S. C. James, S. S. Yoon, *J. Aerosol Sci.* **2012**, *46*, 1.
- [46] S. Su, J. Liang, Z. Wang, W. Xin, X. Li, D. Wang, *Nanoscale* **2020**, *12*, 24450.
- [47] S. Mishra, K. L. Barton, A. G. Alleyne, P. M. Ferreira, J. A. Rogers, *J. Micromech. Microeng.* **2010**, *20*, 95026.
- [48] H. Afsaneh, J. A. W. Elliott, *Langmuir* **2022**, *38*, 13121.
- [49] J. Beroz, A. Hart, J. Bush, *Phys. Rev. Lett.* **2019**, *122*, 244501.
- [50] P. Zhou, H. Yu, W. Zou, Y. Zhong, X. Wang, Z. Wang, L. Liu, *Opt. Express* **2020**, *28*, 6336.
- [51] L. Honaker, A. Sharma, A. Schanen, J. Lagerwall, *Crystals* **2021**, *11*, 687.
- [52] Y. Utsumi, T. Kamei, *Mol. Cryst. Liq. Cryst.* **2004**, *409*, 355.